Spiral waves in nematic liquid crystals: Experimental analysis of selection rules

A. Vierheilig,* C. Chevallard, and J. M. Gilli
Institut Non Linéaire de Nice, UMR 129, CNRS, UNSA, 1361 Route des Lucioles, 06560, Valbonne, France
(Received 17 October 1996)

Archimedian spiral waves develop around umbilics, in an homeotropically anchored nematic sample. They are observed under the influence of a rotating magnetic field in the plane of the glass plates, and in presence of a destabilizing electric field. The geometrical characteristics of these experimental spirals (pitch, rotation frequency, etc.) are analyzed in parameter space. These spiral waves are numerically fitted with Archimedian spirals to good degree of accuracy. The transverse speed of zero curvature Bloch walls are deduced from these measurements. The existing domain of these spiral waves is limited, respectively, toward large (low) magnetic-field rotation speed, or low (large) magnetic-field intensities, by the asynchronous regime (by a Bloch-Ising transition of the walls). These experimental results are compared to two-dimensional interactive simulations of a Ginzburg-Landau equation. The measurements made in the low-field domain (which is a validity condition for the model derivation) confirm the applicability of the same selection criterion deduced by Burton, Cabrera, and Frank [Philos. Trans. R. Soc. London Ser. A **243**, 299 (1951)] for the description of spiral shaped steps in cristalline growth, and more recently for the fronts of excitable media. [S1063-651X(97)12706-4]

PACS number(s): 61.30.Gd, 61.30.Jf, 47.20.Ky

INTRODUCTION

In the main part of this work, the dynamics of spiral pattern in homeotropically aligned nematic liquid crystal layers, above the Fréedericksz transition, is investigated. These spirals, which have been observed for several years, have to our knowledge not been the subject of a systematic quantitative analysis. One recent attempt [1] to fit the selection rules with the experimental results of Ref. [2] is associated with a strong tilt situation which is not in the domain of validity for the Ginzburg-Landau equation used.

In the presence of an in-plane rotating magnetic field, spiral patterns develop around vortices which connect Bloch walls of opposite chirality. The Bloch walls separate the two symmetrical distorted states of the twofold degenerate Fréedericksz transition under a magnetic field. Due to their opposite chirality [3], the two types of Bloch walls propagate [4] in opposite directions, and form a double-armed spiral around the vortex. The topological charge is either $+1$ or -1.

As described in Ref. [5], the experiments were made on a nematic liquid crystal sandwiched between glass plates in a homeotropic alignment. Initially, in the absence of external fields the director $\mathbf{n}$ points along $\hat{z}$ throughout the sample. To observe the formation of spiral patterns, we need to destabilize this homeotropic state. This is done by applying a horizontal magnetic field H and/or a vertical electric field E [since for methoxybenzylidenebutylaniline (MBBA), which is the liquid crystal material used here, the dielectric anisotropy ε_a is negative]. The threshold of this Freedericksz transition [6] is given by $\xi_{\mathrm{Freed}}=1$, where

$$\xi=\left(\frac{\chi_a H^2-\varepsilon_a E^2}{K_3\left(\frac{\pi}{d}\right)^2}\right)^{1/2} \tag{1}$$

where K_3 is the bend elastic constant, and d the thickness of the sample. If the Fréedericksz transition is induced purely by the electric field, we will have an infinite degeneracy in the azimuthal angle of the tilted director.

The tilt angle is a function of ξ and z [see Fig. 1(a)]. In the case of external fields just above the Freedericksz transition ($\xi \gtrsim 1$), only the first Fourier mode becomes unstable, and the square of the tilt angle in the midplane of the sample increases proportionally to $(\xi-1)$. In the case of strong external fields ($\xi \gg 1$), higher Fourier modes are unstable and the tilt angle will be saturated at $\pi/2$ in most of the sample [see Fig. 1(b)].

In the case of a small tilt angle, the system can be modeled by the two-dimensional (2D) perturbed Ginzburg-Landau equation with a complex order parameter [5], using the torque equation

$$\gamma_1 \mathbf{n}\times\partial_t\mathbf{n}=-\mathbf{n}\times\frac{\delta F}{\partial \mathbf{n}},$$

where F is the Frank free energy including coupling to external fields, and γ_1 the rotational viscosity, and assuming that only the first Fourier mode is unstable (small tilt angles), we can derive the following dynamical equation:

$$\gamma_1\partial_t A=\mu A+\gamma\overline{A}e^{2i\nu t}+\frac{K_1+K_2}{2}\nabla^2 A+\frac{K_1-K_2}{2}\overline{A}_{\eta\eta}-a|A|^2A, \tag{2}$$

with

$$\mu=\tfrac{1}{2}\chi_a H^2-\varepsilon_a E^2-K_3\left(\frac{\pi}{d}\right)^2,$$

$$\gamma=\tfrac{1}{2}\chi_a H^2,$$

*Also at Inst. of Physics, Univ. of Bayreuth, D-95440, Germany.

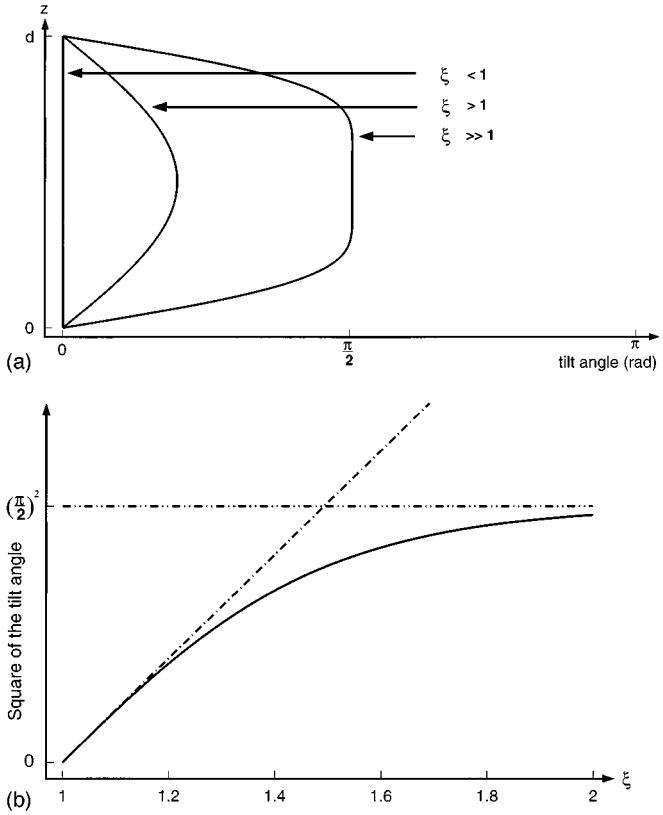

FIG. 1. The inclination angle. (a) The tilt angle of **n** measured from the z axis is plotted as a function of z for different field strengths. (b) The square of the tilt angle at $z=d/2$ is plotted as a function of ξ. From an expansion of the Frank free energy around the Fréedericksz transition, we obtain the slope of the dash-dotted line to be 4 K_3/K_1.

$$a=\tfrac{1}{2}(K_1-\tfrac{3}{2}K_3)\left(\frac{\pi}{d}\right)^2-\tfrac{3}{4}\varepsilon_a E^2,$$

$$\eta=x-iy.$$

ν is the rotation frequency of the magnetic field, and χ_a and ε_a the diamagnetic and the dielectric anisotropies, respectively. The complex order parameter $A=X+iY$ describes the x and y components of the director **n** in the midplane of the sample, with

$$\overline{A}_{\eta\eta}=(\partial_x+i\partial_y)^2(X-iY).$$

The parameters space is a 4D space, with d the thickness of the sample, E and H the respective magnitudes of the electric and magnetic fields, and ν the rotation frequency of the magnetic field. Different regions of the parameter space correspond to different dynamical regimes. In particular, the spiral patterns considered in this paper can only be observed in a parameter space region where Bloch walls exist. This region is limited, toward low rotation frequencies of the magnetic field, and toward high-field strength, by the transformation of Bloch walls into static Ising walls. Conversely, toward high rotation frequencies or low-field strength, the transition to the asynchronous regime, in which the director rotates at lower frequency than the external magnetic field, is not directly associated with the disappearance of spiral

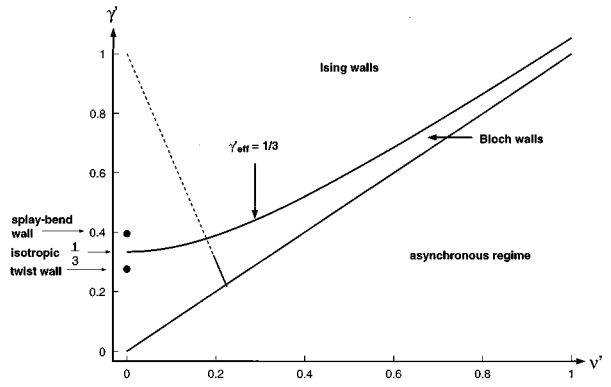

FIG. 2. The transition lines in the parameter space of the perturbed Ginzburg-Landau equation. $\gamma'=\nu'$ is the synchronous-asynchronous transition, and $\gamma'_{\rm eff}=\frac{1}{3}$ is the Ising-Bloch transition. The two dots indicate the static Ising-Bloch transition when taking into account elastic anisotropy. The ratios of the elastic constants correspond to MBBA at room temperature. The simulation performed for comparison with experimental results in Sec. II C are done along the dashed line of the Ginzburg-Landau parameter space: $\gamma'=1-3.48\nu'$.

waves. These last exist as long as the rotation frequency of the spiral is larger than the rotation frequency of the director in the locally rotating coordinate system.

I. GINZBURG-LANDAU THEORY

The Ginzburg-Landau equation (2) can be renormalized to

$$\partial_{t'}A'=A'+\gamma'\overline{A'}e^{2i\nu' t'}+\nabla'^2A'+\delta k\overline{A'}_{\eta'\eta'}-|A'|^2A' \tag{3}$$

by

$$\overline{A}=\left(\frac{a}{\mu}\right)^{1/2},\quad \text{the scale for the order parameter,}$$

$$\tilde{t}=\frac{\gamma_1}{\mu}\quad \text{the characteristic time,}$$

$$\tilde{x}=\left(\frac{K_1+K_2}{2\mu}\right)^{1/2}\quad \text{the characteristic length,}$$

and

$$\gamma'=\frac{1}{\mu}\,\gamma,\quad A'=A/\tilde{A},$$

$$\nu'=\frac{1}{\mu}\,\nu\gamma_1,\quad x'=x/\tilde{x},$$

$$\delta k=\frac{K_1-K_2}{K_1+K_2},\quad \eta'=\eta/\tilde{x},$$

$$t'=t/\tilde{t},$$

In the isotropic approximation ($\delta k=0$) we obtain a 2D parameter space in γ' and ν' (see Fig. 2, and, for more

details, Ref. [5]). There are two main regions of interest:

(i) The asynchronous regime with $\nu' > \gamma'$ (the lower part of Fig. 2) where the order parameter A rotates at a frequency lower than ν. Experimentally this means that the rotation frequency of the magnetic field is too large for the applied field strength and the director cannot follow.

(ii) The synchronous regime with $\gamma' > \nu'$ (the two upper parts of Fig. 2), where the order parameter rotates with frequency ν. Experimentally, the director rotates with the same frequency as the external magnetic field, but with a certain retardation angle.

The synchronous-asynchronous transition is mainly controlled by the rotational viscosity γ_1. Since we are interested in the synchronous regime, we transform Eq. (3) in the locally rotating coordinate system, $A \rightarrow A e^{i\nu' t}$:

$$\partial_t A = (1 + i\nu')A + \gamma' \overline{A} + \nabla^2 A + \delta k \overline{A}_{\eta\eta} e^{-2i\nu' t} - |A|^2 A. \tag{4}$$

With $\delta k = 0$ and $\gamma' \neq 0$, we have two fixed points in the synchronous regime, which lie on the X axis for $\nu' = 0$, and otherwise are dephased by the retardation angle δ, with $\gamma' \sin 2\delta = \nu'$ and $\delta \epsilon [0; \pi/4]$. For analytical treatment it is convenient to perform another local rotation of the order parameter in the ''phase-shifted'' coordinate system $A \rightarrow A e^{i\delta}$. In the isotropic approximation, the real and imaginary part of the order parameter A become

$$\partial_t X = (1 + \gamma'_{\text{eff}})X - 2\nu' Y + \nabla^2 X - (X^2 + Y^2)X,$$

$$\partial_t Y = (1 - \gamma'_{\text{eff}})Y + \nabla^2 Y - (X^2 + Y^2)Y, \tag{5}$$

with $\gamma'_{\text{eff}} = \sqrt{\gamma'^2 - \nu'^2} = \gamma' \cos 2\delta$. The two fixed points of Eq. (5) are $A = \pm\sqrt{1 + \gamma'_{\text{eff}}}$.

In the upper region of Fig. 2, the heteroclinic orbit connecting in space the two fixed points is called an Ising wall:

$$A_{\text{Ising}} = \sqrt{1 + \gamma'_{\text{eff}}} \tanh \frac{x}{x_0}, \tag{6}$$

with $x_0 = \sqrt{2/(1 + \gamma'_{\text{eff}})}$.

At $\gamma'_{\text{eff}} = \frac{1}{3}$, the Ising wall becomes unstable, and transforms for decreasing γ' into a Bloch wall. This describes a different kind of heteroclinic orbit. This transition is a pitchfork bifurcation. An appropriate order parameter of the Ising-Bloch transition is the chirality $\chi = \pm\sqrt{1 - 3\gamma'_{\text{eff}}}$. At the transition there is a twofold degeneracy between Bloch walls of either positive or negative chirality. Analytically, there exist only perturbative solutions for Bloch walls near the transition from Ising walls:

$$A_{\text{Bloch}} = \sqrt{1 + \gamma'_{\text{eff}}} \tanh \frac{x}{x_0} + i \frac{\chi}{\cosh \dfrac{x}{x_0}}. \tag{7}$$

In the rotating case ($\nu' \neq 0$), the Bloch walls propagate, and at first order in χ the velocity c of a straight wall is [3,5,7]

$$c = \frac{3\pi}{2\sqrt{2}} \frac{\chi \nu'}{1 + \gamma'_{\text{eff}}} \sim \chi. \tag{8}$$

Bloch walls of opposite chirality are connected via Néel-point-type vortices of topological charge $S = \pm 1$. Near the Ising-Bloch transition the solution reads [7]

$$A_{\text{Néel}} = \sqrt{1 + \gamma'_{\text{eff}}} \tanh \frac{x}{x_0} + i \frac{\chi}{\cosh \dfrac{x}{x_0}} \tanh\left(\frac{y}{r_0}\right), \tag{9}$$

with $r_0 = 2/\sqrt{1 - 3\gamma'_{\text{eff}}}$.

Since the Néel-point-type vortices connect two Bloch walls of opposite chirality, they propagate in the rotating case in opposite directions. A double-armed spiral forms around the vortex, where r_0 gives approximately the size of the spiral core.

If we take into account the elastic anisotropy, the threshold of the Ising-Bloch transition becomes a function of the angle between the interface and the magnetic field. Analytical expressions exist only for $\nu' = 0$ and the two extreme cases called splay-bend walls (the interface is perpendicular to the magnetic field) and twist walls (the interface is parallel to the magnetic field). From Ref. [5] the threshold of the static Ising-Bloch transition becomes

$$\gamma'_{IB} = \alpha \quad \text{with} \quad \alpha = \frac{(\sqrt{1 + 8\beta} + 1)^2}{16\beta - (\sqrt{1 + 8\beta} + 1)^2}, \tag{10}$$

where $\beta = K_1/K_2$ for splay-bend walls and $\beta = K_2/K_1$ for twist walls in the approximation of $K_1 = K_3$. For interfaces with an angle different from 0 or $\pi/2$, the threshold value γ'_{IB} lies in between the two above limits.

Using the elastic constants given in Sec. II A for MBBA at room temperature, we obtain $\beta = \frac{3}{2}$ and $\alpha \approx 0.394$ for splay-bend walls, and $\beta = \frac{2}{3}$ and $\alpha \approx 0.275$ for twist walls (see Fig. 2).

One can associate the 2D parameter space of Eq. (4) (ν', γ') with the experiment. They are *a priori* 4D, with d the thickness of the cell, E the electric field, H the magnetic field, and ν the rotation frequency of the magnetic field [see Eq. (2)]. However, E and d can be reduced to a single variable and one obtains a three-dimensional parameters space in H, ν and σ [see Figs. 3(a) and 3(b)], where

$$\sigma = -\epsilon_a E^2 - K_3 \left(\frac{\pi}{d}\right)^2.$$

Tracing H^2 as a function of ν, with σ as a parameter, one finds four transition lines:

$$(1) \quad H^2 = -\frac{1}{\chi_a}\left(\frac{(\gamma_1 \nu)^2}{\sigma} + \sigma\right) \text{ with } \sigma < 0,$$

the Fréedericksz transition to the synchronous regime (pitchfork bifurcation);

$$(2) \quad H^2 = -\frac{2}{\chi_a}\sigma \text{ with } \sigma < 0,$$

the Fréedericks transition to the asynchronous regime (Hopf bifurcation);

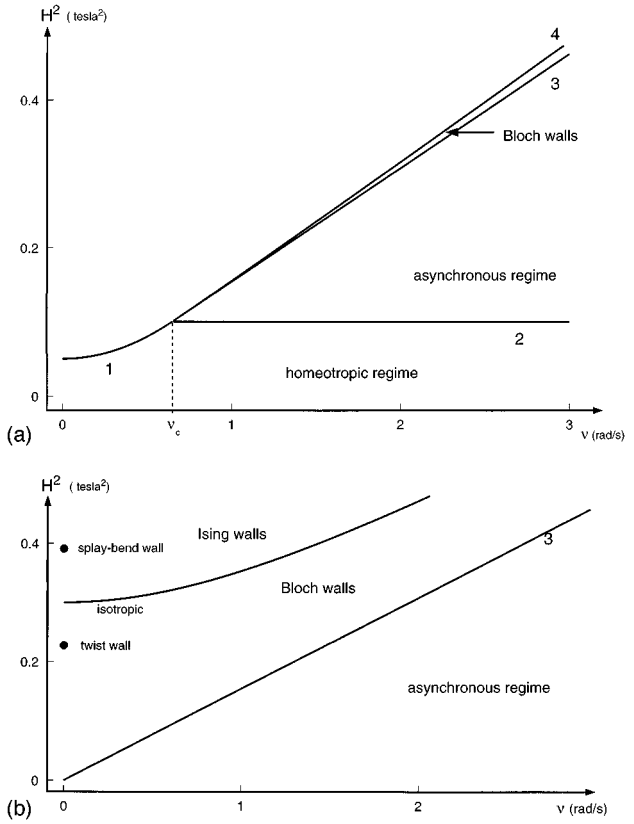

FIG. 3. The theoretical transition lines in the experimental parameter space. (a) $\sigma=-0.05$ (corresponding to the case $E<E_F$). (b) $\sigma=0.3$.

$$(3)\quad H^2=\frac{2}{\chi_a}\gamma_1\nu \text{ (independent of } \sigma),$$

the synchronous-asynchronous transition; and

$$(4)\quad H^2=\frac{1}{4\chi_a}\left(\sigma+3\sqrt{\sigma^2+8(\gamma_1\nu)^2}\right)\widetilde{\nu\gg}\frac{\sigma}{\gamma_1}\frac{3\sqrt{2}}{4}\frac{2}{\chi_a}\gamma_1\nu,$$

the Ising-Bloch transition (pitchfork bifurcation). The two types of Fréedericksz transitions exist only for $\sigma<0$ ($\Leftrightarrow E<E_F$) and

$$\nu_c=-\frac{\sigma}{\gamma_1}\quad\text{with}\quad\sigma<0.$$

For $\sigma>0$, Bloch walls are stable for $\nu=0$ [see Fig. 3(b)]. This considerably facilitates experimental manipulations. Note that the synchronous-asynchronous transition depends neither on the applied electric field nor on the cell thickness. With the elastic anisotropy, the static Ising-Bloch transition becomes

$$H^2=\frac{2}{\chi_a}\frac{\alpha}{1-\alpha}\sigma, \tag{11}$$

where α is defined in Eq. (10).

II. EXPERIMENT

A. Setup

The experimental setup used is similar to ones described in Ref. [5]. The probe consists of two glass plates containing the liquid crystal. The inner surfaces are faced with indium-tin-oxide, a transparent conductor, allowing the application of an electric field normal to the glass plates. A high-frequency ac voltage of 5 kHz is used to avoid space-charge creation and electrohydrodynamic effects. Since the dielectric anisotropy of MBBA is negative, the electrical field serves to destabilize the homeotropic state.

The inner surfaces of the glass plates are treated with lecithin, which provides a homeotropic anchoring. The spacers between the two glass plates were 3.5–75 μm thick. Typical values for the material parameters for MBBA at room temperature are:

$$\chi_a=\frac{4\pi\chi_{a,\mathrm{cgs}}}{\mu_0}=1\,\frac{\mathrm{A\ m}}{\mathrm{V\ s}}\quad\text{magnetic anisotropy,}$$

$$\epsilon_a=\varepsilon_{a,\mathrm{cgs}}\varepsilon_0=-6.195\times10^{-12}\,\frac{\mathrm{A\ s}}{\mathrm{V\ m}}\quad\text{dielectric anisotropy,}$$

$$K_1=6.0\times10^{-12}\ \mathrm{N}\quad\text{splay-elastic constant,}$$

$$K_2=4.0\times10^{-12}\ \mathrm{N}\quad\text{twist-elastic constant,}$$

$$K_3=7.5\times10^{-12}\ \mathrm{N}\quad\text{bend-elastic constant,}$$

$$\gamma_1=7.7\times10^{-2}\ \mathrm{N\ s\ m^{-2}}\quad\text{rotational viscosity,}$$

$$[H]=\mathrm{tesla}=\frac{\mathrm{V\ s}}{\mathrm{m}^2},$$

$$[E]=\frac{\mathrm{V}}{\mathrm{m}},$$

where the notation H for the magnetic induction is kept.

However, measurements performed by different groups do not always coincide (Ref. [6], Table 3.2), and the value for the rotational viscosity γ_1, which controls the synchronous-asynchronous transition, changes strongly when varying the temperature near ambient [8].

The probe is fixed above the gap between two permanent magnets, mounted on a turnable disc (see Fig. 4). The magnetic-field strength is controlled by varying the distance between the sample and the magnets. On the symmetry axis, a horizontal field of up to 7 kG is applied near the magnets. Gradients are encountered up to 500 G/mm in the vertical direction.

The probe is placed between crossed polarizer and analyzer. The birefringence of the liquid crystal is used to observe the spiral pattern. A device is added, allowing us to turn the polarizer and analyzer to the same frequency as the magnetic field. This is used in order to keep the angle between the polarized light and the director constant, while being in the synchronous regime. This provides an image of constant contrast, which is useful for the image analysis.

Other experimental setups have been proposed [2,4], but this one has the advantage that single vortices of the desired

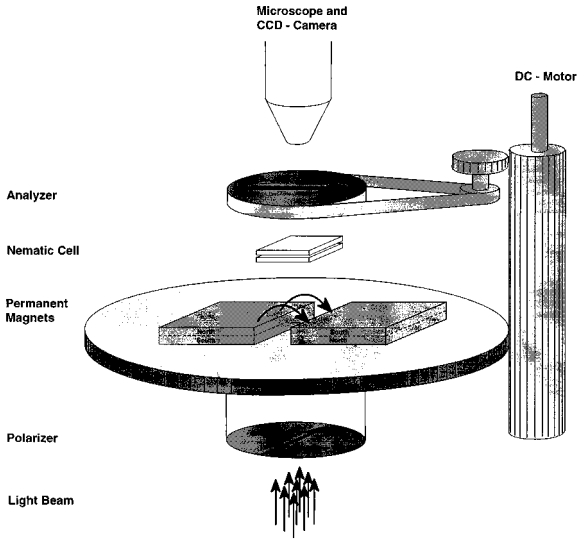

FIG. 4. The experimental setup.

sign can easily be created. The use of permanent magnets leads, especially in the range of high magnetic fields, to large gradients, which causes uncertainties in the strength of the magnetic field. Additionally, high-field strengths are encountered only when bringing the sample near the magnets. This makes it difficult to add a temperature control device.

In our experiment we use MBBA since it has, in comparison with other nematic liquid crystals, a large magnetic anisotropy. It is thus possible to perform the experiment in this relatively simple setup, since permanent magnets are sufficient as a field source. However, MBBA is subject to a degradation process in the presence of H_2O (Schiff base). This is nearly inevitable due to the humidity of the air. The degradation of the liquid crystal causes a decrease of the threshold temperature of the nematic-isotropic transition which results in a decrease of the rotational viscosity γ_1 and the three elastic constants.

For anchoring on the glass plates the organic material lecithin is used. It is also susceptible to degradation. This results in weaker surface anchoring of the director [9]. These degradation processes will influence the behavior of the spiral pattern, especially near the Freedericksz transition, which is controlled by the elastic constant for bend deformation K_3 and the strength of the surface anchoring.

B. Spiral analysis

The analysis of the spirals consists of two steps. The first one is to record series of images of the spiral as a function of time, and the second one is to fit each spiral to an Archimedian form, which allows one to determine the wavelength λ and the rotation frequency ω. The program uses the SCREEN MACHINE II card, to display the live video of the camera on the screen. It allows one to grab the single images of one series either by hand or automatically at a fixed rate, where the maximum rate of the acquisition card is about one image per five seconds.

The next step consists of finding the spiral arm, and is followed by a fit into an Archimedian form. In the experiment the spiral arm, which is a curved, moving Bloch wall,

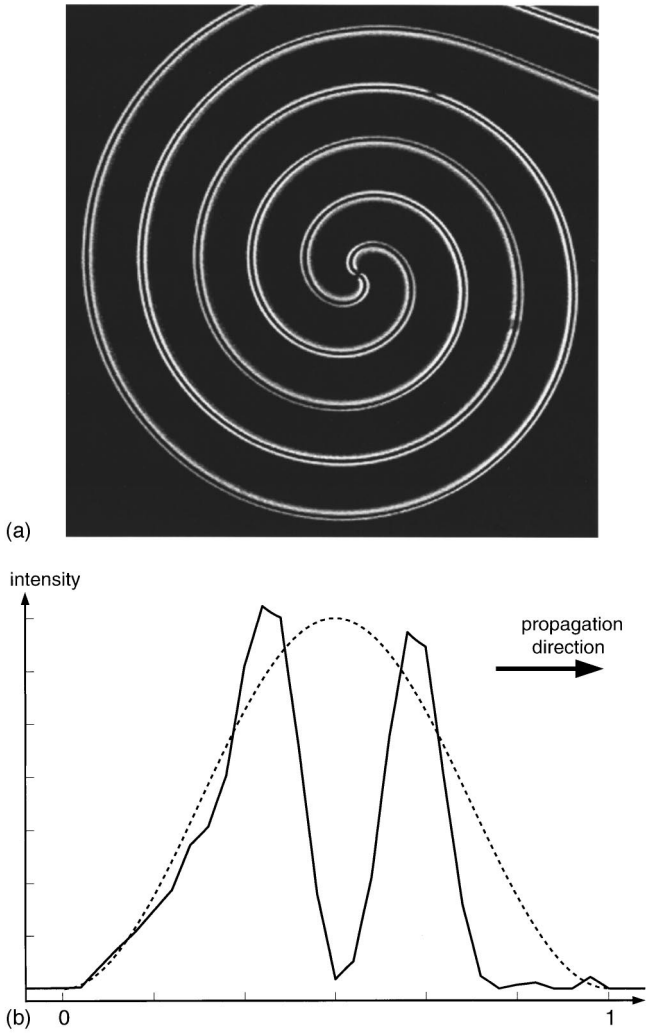

FIG. 5. Experimental picture and intensity of a spiral arm. (a) A typical image of the spirals observed in the liquid crystal (3×3 mm^2). (b) The intensity plot when crossing perpendicularly a spiral arm, approximated by $F(x)$.

is bright against the background, possibly with a very small dark area in the middle [see Fig. 5(a)]. The intensity profile when crossing the spiral arm perpendicularly can be approximated by $F(x)=A_0[1-\cos(2\pi(x-x_0))]$, where x and x_0 are renormalized by the width of the spiral arm, A_0 is the amplitude, and x_0 is the displacement which gives the center of the arm [see Fig. 5(b)].

If we project $F(x)$ onto the double period

$$c_{1/2}=\int_0^1 dx\ F(x)\cos(\pi x)=-A_0\,\frac{4}{3\pi}\sin(2\pi x_0)$$

and onto the fundamental mode

$$c_0=\int_0^1 dx\ F(x)=A_0,$$

we obtain

$$x_0=\frac{1}{2\pi}\arcsin\left(-\frac{4}{3\pi}\,\frac{c_{1/2}}{c_0}\right)$$

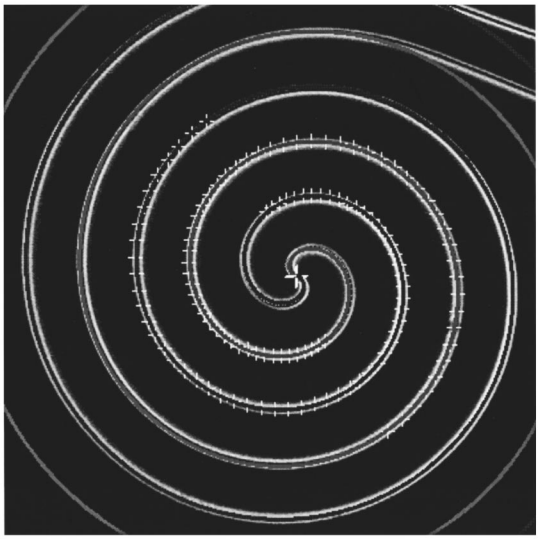

FIG. 6. Archimedian fit. The spiral of Fig. 5(a) fitted with an Archimedian spiral ($3\times3\ \mathrm{mm}^2$).

The actual intensity at a given position is interpolated from the four pixels surrounding it. By default we use five interpolations per pixel, but this can be adjusted by the user.

This procedure is repeated while turning with a step size defined by the user around an approximate center given by the user and using the newly found position of the spiral arm as radial distance. The program thus follows the spiral towards its center.

These points are then fitted to an Archimedian form $r_0(\theta)=(\lambda/2\pi)(\theta-\theta_0)$, where we have four unknown variables: the wavelength λ, the initial angle θ_0, and the position of the center $\mathbf{r}_0$. Since one of the unknown variables is periodic, there exists no analytical expression to calculate them, and we use an iterative method.

The first step is to transform the points from Cartesian coordinates to polar coordinates around a preliminary center, and to perform a linear regression on the thus-obtained function $r(\theta)$. This gives us the preliminary wavelength λ' and initial angle θ_0'. The function $G(\theta)=r(\theta)-(\lambda'/2\pi)(\theta-\theta_0')$ will have periodic oscillations with a period of 2π, depending in size and phase on the displacement $\delta\mathbf{r}$ of the preliminary center. Supposing $|\delta\mathbf{r}|\ll\lambda$, for the two components of the displacement $\delta\mathbf{r}$ we obtain

$$\delta x=-\frac{1}{\pi n}\int_{\theta}^{\theta+2\pi n}d\theta\ G(\theta)\cos\theta,$$

$$\delta y=-\frac{1}{\pi n}\int_{\theta}^{\theta+2\pi n}d\theta\ G(\theta)\sin\theta,$$

where n is an integer.

This procedure is repeated until $|\delta\mathbf{r}|$ lies below an upper boundary (actually a thousand pixels). These fits are done on the two arms of the double-armed spiral and on each image of the series (see Fig. 6). At the end of the series, linear regressions are done to calculate the mean value of the wavelength λ, the rotation frequency ω, and the angular separation of the two spiral arms.

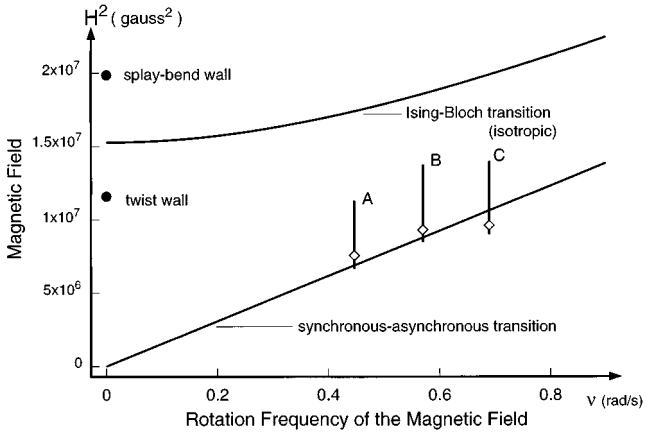

FIG. 7. The parameter space. The lines for the Ising-Bloch and the synchronous-asynchronous transition are taken from theory. The three vertical lines are the measurements performed for three rotation frequencies of the magnetic field ν_A, ν_B, and ν_C. The diamonds indicate the experimentally found asynchronous-synchronous transition, and the upper ends of the lines are the beginning of the Ising-Bloch transition. The heavy dots indicate the theoretical static Ising-Bloch transition for a splay bend and a twist wall.

Since we expect deviations from the purely Archimedian spiral near the core [10], the points we use for the fit are taken in the far field of the spiral. Nevertheless the deviation from the Archimedian spiral near the core remains small in general.

C. Experimental determination of the transition lines in the parameter space

The Ginzburg-Landau equation, which is used for modeling the experiment, supposes small inclination angles of the director from the initially homeotropic state. In order to validate the model, we tried to use a destabilizing electric field just above the Freedericksz transition, small magnetic fields, and low rotation frequencies. In this range, due to the low velocities of the Bloch walls, the experiment becomes very time consuming, and during the experiment temperature changes of up to 2 °C occurred around a mean value of 21 °C due to the heating of the microscope.

For the experimental data given in the following, thickness of the sample was 23 μm and the voltage 5 V_{eff}. With a magnetic field of about 3 kG, this corresponds to $\xi\approx1.6$ in Eq. (1). Thus even at this relatively low field strengths the director in the midplane of the sample is already strongly inclined, but still lower field strengths caused experimental problems.

We did three series of measurements, each for a spiral with a $+1$ vortex and a -1 vortex core, where we kept the rotation frequency of the magnetic field ν constant and varied the magnetic field strength H (see Figs. 7 and 8). The maximum field strength is given by the beginning of the Ising-Bloch transition of parts of the spiral arms. Because of the elastic anisotropy, this transition depends on the angle between the Bloch wall interface and the magnetic field [5], and the parts of the spiral arms parallel to the magnetic field will transform to Ising walls at lower field strength. In Fig. 7,

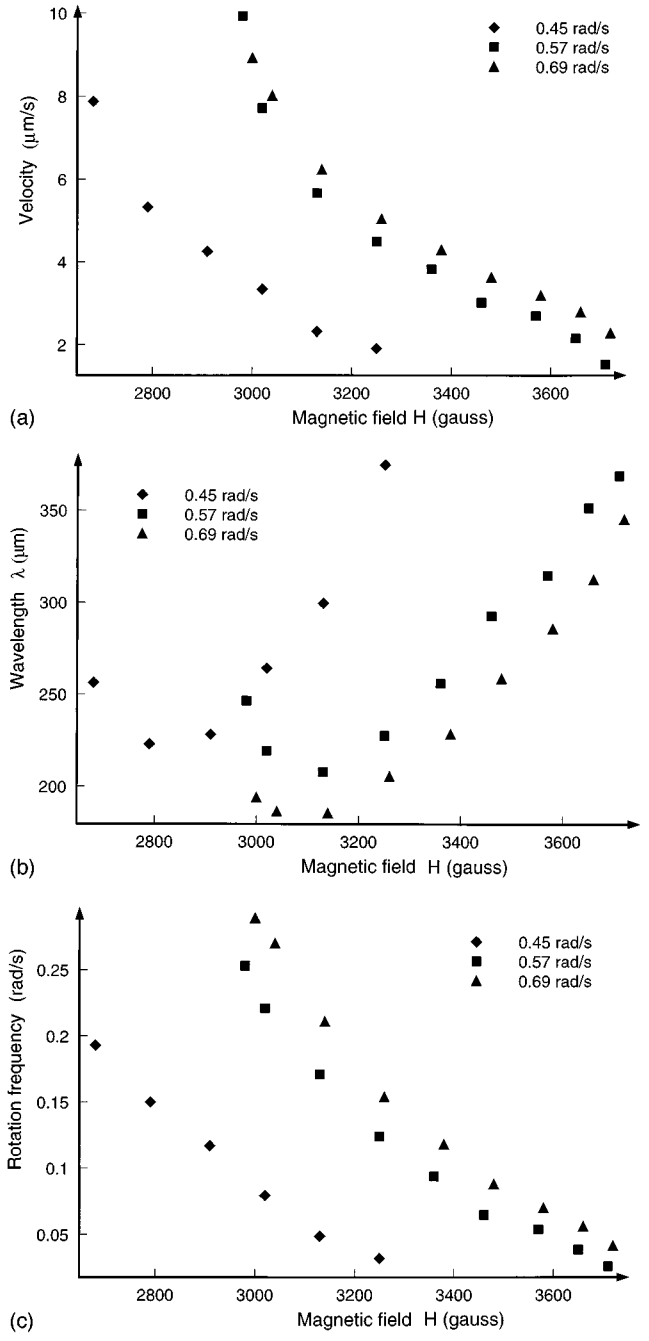

FIG. 8. Experimental data. (a) The velocity of a straight wall c. (b) The selected wavelength λ. (c) The rotation frequency ω, as a function of the magnetic-field strength H. The applied tension is $U=5V_{\text{eff}}$, and the cell thickness is $d=23\ \mu$m. These experimental points correspond to spirals with $a+1$ defect in the core.

the two dark points indicate the theoretical static Ising-Bloch transitions for splay-bend and twist walls. On the other hand, the elastic anisotropy does not influence the synchronous-asynchronous transition, and the data found experimentally provide a comparison with theory.

The threshold values for the synchronous-asynchronous transition, associated with the minimum selected wavelength (and to the phase slip of the director relative to the magnetic field) are in good agreement with theoretical predictions (see Figs. 7 and 8].

Spiral patterns exist even in the asynchronous regime, as long as the rotation frequency of the spiral ω is larger than the rotation frequency of the director (in the rotating coordinate system) $2\pi/T$ with [11]

$$T=\frac{2\pi}{\left[\nu^2-\left(\frac{\frac{1}{2}\chi_a H^2}{\gamma_1}\right)^2\right]^{1/2}}$$

the time for a 2π rotation of the director, and ν the rotation frequency of the magnetic field.

Spirals with $+1$ vortex and -1 vortex cores differ in the selected wavelength λ and in the rotation frequency ω up to 20%. The spiral around a vortex -1 selects a larger wavelength and a smaller rotation frequency (see Fig. 9): due to the anisotropy of elasticity, vortices $+1$ and -1 have different elastic energies which results in different core sizes.

When decreasing the magnetic-field strength and passing into the asynchronous regime, we observe a characteristic increase in the wavelength, and, with increasing rotation frequency of the magnetic field, the wavelength at the synchronous-asynchronous transition decreases.

The velocity of a straight wall $c=(1/2\pi)\lambda\omega$, which we can deduce from the wavelength and the rotation frequency of the spiral, should obviously be equal for the two types of spiral. In our measurement, this has not been exactly the case due to the above-mentioned experimental difficulties.

For $\nu_B\approx 0.57$ rad/s we performed numerical simulations of Eq. (4). Due to low differences between $+1$ and -1 spirals in the simulation, we left out the term accounting for the elastic anisotropy. We transformed the experimental parameters in the two-dimensional parameter space of Eq. (4), which leads to [see Eq. (3)].

$$\gamma'=\nu'\,\frac{\varepsilon_a E^2+K_3\left(\frac{\pi}{d}\right)^2}{\nu\gamma_1}+1\approx 1-3.48\nu',$$

with $\nu'=0.195,\ldots,0.227$ and $\gamma'=0.209,\ldots,0.321$ (see Fig. 2). The synchronous-asynchronous transition is at $\nu'=\gamma'\approx 0.2231$ and the experimental data are reduced to nondimensional units. We obtain good agreement between the simulation and the experimental data and the smallest wavelength at the synchronous-asynchronous transition [see Figs. 9(a)–9(c)].

D. Verification of the Gibbs-Thomson relation

We checked the validity of the Gibbs-Thompson relation for the velocity of a curved Bloch wall:

$$c_n=c-D\chi, \tag{12}$$

with c_n the normal velocity, c the velocity of an uncurved wall, D the orientational diffusion constant, and χ the local curvature.

In the case of a circle-shaped interface the curvature χ equals the inverse of the radius. We measured the radius of

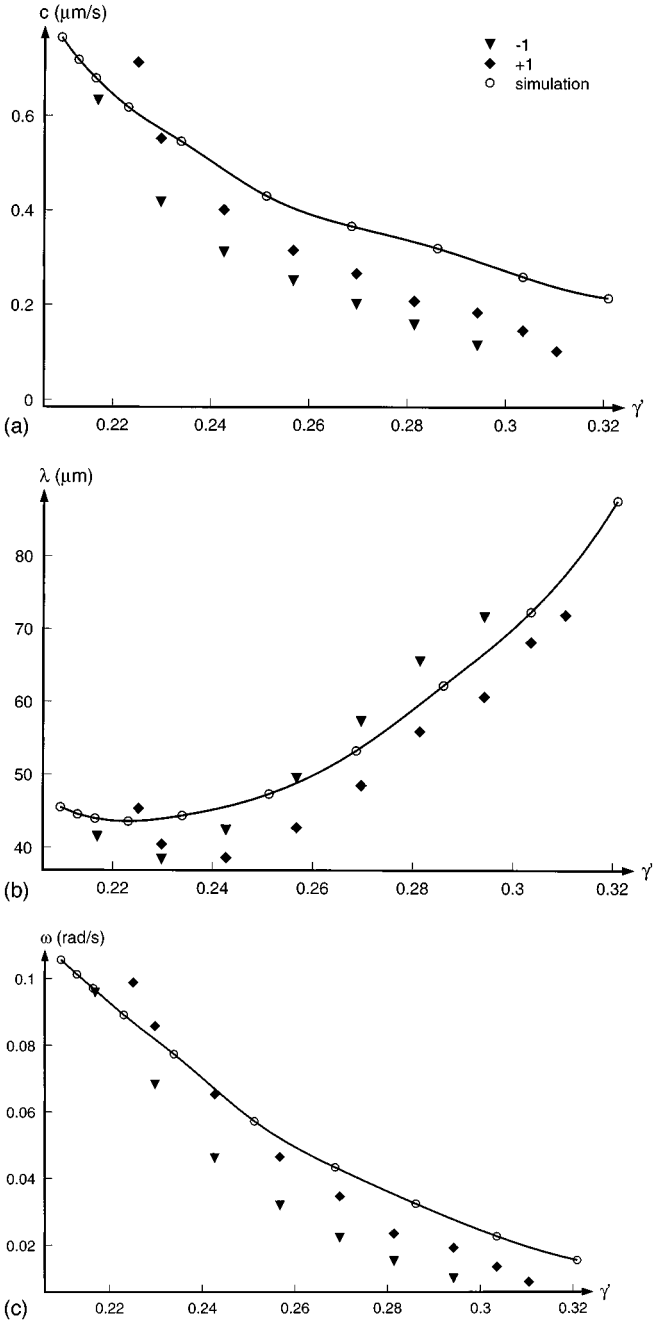

FIG. 9. Comparison between numerical simulations and experimental data. Experimental data are the reduced data corresponding to Figs. 8(a), 8(b), and 8(c), with $\nu_B \approx 0.57$ rad/s and with -1 vortex associated results added.

such a circle-shaped outward-moving Bloch wall as a function of time, from where we can derive the velocity c_n as a function of the curvature χ.

The experimental data show the expected linear behavior (see Fig. 10). A linear regression gives a diffusion constant of $D=76.3\ \mu\text{m}^2/\text{s}$, which is in rather good agreement with the expected diffusion constant $D=(K_1+K_2)/2\gamma_1 \approx 64.9\ \mu\text{m}^2/\text{s}$.

III. FREQUENCY SELECTION RULES

If we take the experimental data, corresponding to the synchronous regime, for the three series of measurements

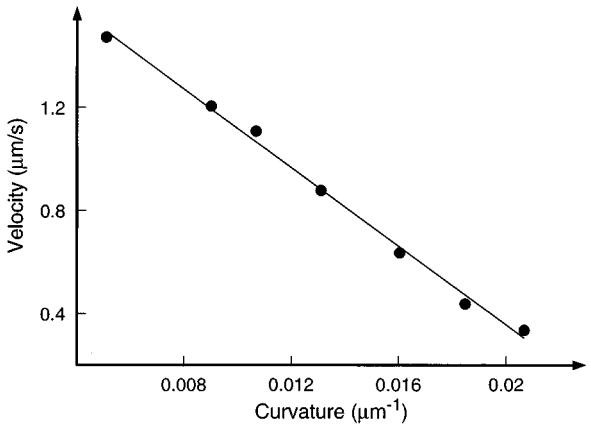

FIG. 10. The Gibbs-Thompson relation. The velocity c_n of a circle-shaped outward-moving interface, and the linear regression.

done at low-field strength for both vortex $(+1)$ and vortex (-1), we see that, in the k^2-ω space with $k=2\pi/\lambda$, the data collapse close to a unique curve (see Fig. 11). This behavior can be understood with the help of the simple geometrical model developed in the early 1950s by Burton, Cabrera, and Frank (BCF) [12] to describe the selection rules of the spiral-shaped steps arising in crystalline growth. In this model, the Archimedian spirals parameters are only controlled by the Gibbs-Thomson relation, without taking into account the influence of a possible spiral core size variation.

From this model we obtain

$$\omega = \frac{D}{m} k^2,$$

where $m \cong 0.331$. The full line of Fig. 11 corresponds to this model associated with the diffusion constant expected in our experimental conditions, and is in good agreement with our measurements. This model is also in agreement with experimental observations of spiral waves in the Belousov-Zhabotinsky reaction, where at least ω/k^2 is constant [13].

In a recent work [14], one of us developed a model to take into account the influence of the core size variation which is

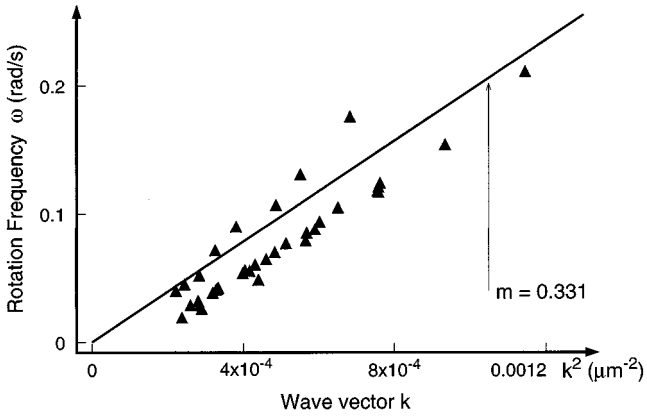

FIG. 11. Frequency selection. The experimental data with low-field strength in k^2-ω space. The slope of the line is D/m, with $D \approx 64.9\ \mu\text{m}^2/\text{s}$.

predicted in the frame of a Ginzburg-Landau approach. A deviation from the BCF model is expected in the small-wavelength domain. Unfortunately the experimental observation of such a deviation would probably be only possible at unrealistic high magnetic-field strength and for very thin samples. Our system does not allow us to reach this parameters domain, and no substantial deviations relative to the BCF model are visible.

CONCLUSION

In this work, we have investigated the geometrical properties of experimental spiral waves, induced by a rotating magnetic field, in a nematic sample undergoing the homeotropic Fréedericksz transition. This kind of numerical fit, done on the polarizing microscope images, has been also done on numerical images, obtained from interactive simulations of a Ginzburg-Landau equation, directly derived from the nematic basic Frank free-energy expression and torque equilibrium equation. Both real and numerical measurements are in good quantitative agreement in the domain of parameters accessible to our experimental setup.

The experimental data plotted in the k^2-ω space all lie along a single line of definite slope, in agreement with the simple geometrical model of Burton-Cabrera-Frank having only the diffusion constant as free parameter: this behavior seems consequently to be in common with systems as different as the excitable waves of the Belouzov-Zhabotinsky reaction or the spiral-shaped steps observed in crystalline growth. Deviations from this simple selection rule, associated with the umbilic core size variations, which are predicted in the ground of a Ginzburg-Landau approach, and observable in simulations of the previous equation, are not accessible to our experiment.

ACKNOWLEDGMENTS

We gratefully acknowledge J. M. Flesselles for help concerning the spiral fit numerical procedure; L. Dupont, who realized the numerical tools of the Ginzburg-Landau simulations; S. Rica and E. Hamm for helpful discussions; the DRET administration (94-2610A); and the University of Nice for financial support.

[1] I. S. Aranson, Phys. Rev. E **51**, R3827 (1995).
[2] K. B. Migler and R. B. Meyer, Phys. Rev. Lett. **66**, 1485 (1991); Physica D, **71**, 412 (1994); K. B. Migler, Ph.D. thesis, Brandeis University, Boston, 1991.
[3] P. Coullet, J. Lega, B. Houchmanzadeh, and J. Lajzerowicz, Phys. Rev. Lett. **65**, 1352 (1990); P. Coullet, J. Lega, and Y. Pomeau, Europhys. Lett. **15**, 221 (1991).
[4] S. Nasuno, N. Yoshimo, and S. Kai, Phys. Rev. E **51**, 1598 (1995).
[5] J. M. Gilli, M. Morabito, and T. Frisch, J. Phys. (France) II **4**, 319 (1994); T. Frisch, Physica D 84, 601 (1995); T. Frisch, S. Rica, P. Coullet, and J. M. Gilli, Phys. Rev. Lett. **72**, 1471 (1994).
[6] P. G. de Gennes and J. Prost, *The Physics Of Liquid Crystals* (Clarendon, Oxford, 1993).
[7] S. Rica, Ph.D. thesis, INLN, University of Nice, 1994.
[8] J. Prost and H. Gasparoux, Phys. Lett. **36A**, 245 (1971).
[9] A. Rapini and M. Papoular, J. Phys. (Paris) Colloq. **4**, C-S4 (1969).
[10] J. J. Tyson and J. P. Keener, Physica D **32**, 327 (1988).
[11] L. Leger-Quercy, Ph.D. Thesis, Université Paris-Sud, Orsay, 1976.
[12] W. K. Burton, N. Cabrera, and F. C. Frank, Philos. Trans. R. Soc. London Ser. A **243**, 299 (1951).
[13] A. Belmonte and J. M. Flesselles, Phys. Rev. Lett. **77**, 1174 (1996); A. Belmonte, Q. Ouyang, and J. M. Flesselles, J. Phys. (France) II (to be published).
[14] E. Hamm, S. Rica, and A. Vierheilig (unpublished).